Kinetic Monte Carlo simulation of self-organized pattern formation induced by ion beam sputtering using crater functions

Zhangcan Yang,[1,2] Michael A. Lively,[1] and Jean Paul Allain[1,*]

[1]*University of Illinois at Urbana-Champaign, Department of Nuclear, Plasma, and Radiological Engineering, Urbana, Illinois 61801, USA*

[2]*University of Tennessee, Department of Nuclear Engineering, Knoxville, Tennessee 37996, USA*

(Received 19 June 2014; revised manuscript received 12 October 2014; published 26 February 2015)

The production of self-organized nanostructures by ion beam sputtering has been of keen interest to researchers for many decades. Despite numerous experimental and theoretical efforts to understand ion-induced nanostructures, there are still many basic questions open to discussion, such as the role of erosion or curvature-dependent sputtering. In this work, a hybrid MD/kMC (molecular dynamics/kinetic Monte Carlo) multiscale atomistic model is developed to investigate these knowledge gaps, and its predictive ability is validated across the experimental parameter space. This model uses crater functions, which were obtained from MD simulations, to model the prompt mass redistribution due to single-ion impacts. Defect migration, which is missing from previous models that use crater functions, is treated by a kMC Arrhenius method. Using this model, a systematic study was performed for silicon bombarded by Ar^+ ions of various energies (100 eV, 250 eV, 500 eV, 700 eV, and 1000 eV) at incidence angles of 0° to 80°. The simulation results were compared with experimental findings, showing good agreement in many aspects of surface evolution, such as the phase diagram. The underestimation of the ripple wavelength by the simulations suggests that surface diffusion is not the main smoothening mechanism for ion-induced pattern formation. Furthermore, the simulated results were compared with moment-description continuum theory and found to give better results, as the simulation did not suffer from the same mathematical inconsistencies as the continuum model. The key finding was that redistributive effects are dominant in the formation of flat surfaces and parallel-mode ripples, but erosive effects are dominant at high angles when perpendicular-mode ripples are formed. Ion irradiation with simultaneous sample rotation was also simulated, resulting in arrays of square-ordered dots. The patterns obtained from sample rotation were strongly correlated to the rotation speed and to the pattern types formed without sample rotation, and a critical value of about 5 rpm was found between disordered ripples and square-ordered dots. Finally, simulations of dual-beam sputtering were performed, with the resulting patterns determined by the flux ratio of the two beams and the pattern types resulting from single-beam sputtering under the same conditions.

DOI: 10.1103/PhysRevB.91.075427 PACS number(s): 79.20.Rf, 81.16.Rf, 68.35.Ct

I. INTRODUCTION

Various self-organized patterns including ripples and quantum dots can be formed on surfaces by ion beam sputtering (IBS) [1–7]. For the past few decades, understanding of this phenomenon has mainly relied on the Bradley-Harper (BH) theory [1], which attributes the formation of self-organized patterns to the interplay between roughening by curvature-dependent erosion and smoothening by thermally activated surface diffusion.

Recently, the development of crater function theory has challenged this erosion-based paradigm with a new one based on mass redistribution. The theory has shown that erosion is overwhelmed by mass redistribution at low incidence and intermediate angles in the pattern formation [8]. Despite its success in explaining the absence of ripple formation under low angle incidence, there are still some questions open to discussion. For example, even though the inclusion of mass redistribution provides a convincing explanation for the flat-to-ripple transition [8], the underlying mechanism for the transition of ripple orientation at glancing angle is still unknown. The traditional BH theory asserts that curvature-dependent erosion determines ripple orientation [1]. The mass-redistribution-based theory did not predict a transition to perpendicular-mode ripples at high angles, explained by either the absence of curvature dependence, shadowing effects, or surface channeling in the model [8]. Although Hossain and coworkers [9] asserted that mass redistribution is able to explain formation of perpendicular-mode ripples at glancing angles, the incorrect prediction of perpendicular-mode ripples at small angles, which were reported in experiments [10] but later corrected due to multiple scattering effects [11], makes their conclusion open to debate. More recently, an analysis of experimental data [12] showed that the constraints implied by the moment-based theory could not be applied to experimental measurements of the curvature coefficients, although it was shown by further theoretical analysis [13] that this inconsistency could arise from the neglect of curvature dependence. In any case, it appears that the moment-based theory is not a complete explanation of surface evolution under ion bombardment, and the role of sputtering in ion-induced pattern formation remains an open question.

The recently developed moment-based theory by Norris has additional practical shortcomings. First, it is only valid for the early stage bombardment due to the assumption of a small surface slope and the truncation to first order. As the surface becomes rougher, the nonlinear or higher-order terms may become important. For instance, the current moment-based theory cannot predict ripple amplitude saturation or ripple coarsening in the nonlinear regime. Second, the current continuum theories cannot easily model pattern formation on arbitrary

*Corresponding author: allain@illinois.edu

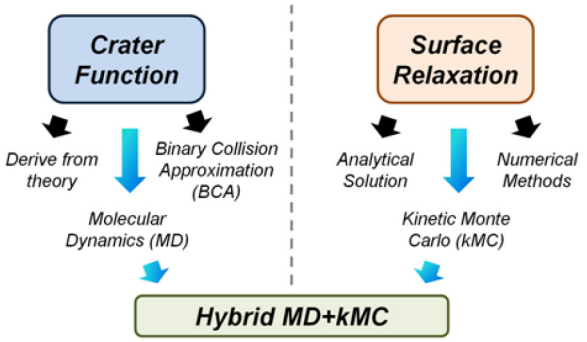

FIG. 1. (Color online) Graphical representation of the model presented in this work, placing it into its proper context and showing the differences compared to previous approaches.

surfaces. In most experimental studies, smooth commercial wafers are used. However, for practical applications the initial surfaces may either be smooth or already have features. In the latter case, linear continuum theories are not applicable due to the breakdown of small slope assumption. Third, the absence of shadowing effects and redeposition in existing continuum theories has weakened their validity for glancing incidence angles or for predicting steep, tall structures. Last but not least, continuum theories ignore the surface defect kinetics under irradiation, which have been shown to play an important role in surface morphology evolution [14–16].

The hybrid MD/kMC (molecular dynamics/kinetic Monte Carlo) model developed in this work is differentiated from previous atomistic simulations [15–21] primarily by the use of the crater functions to treat ion impacts. This model uses craters to consider the prompt mass redistribution due to single-ion impacts. On the other hand, this model is differentiated from previous work using MD craters [9,22] by the use of a kMC Arrhenius model of surface defect migration to consider the gradual smoothening of the surface. Figure 1 shows graphically how the treatment given in this model differs from previous work and places the present work in context.

Previous work with this model [23] has demonstrated its usefulness for studying pattern formation. The results have shown that the absence of ripple formation at low angles is due to mass redistribution rather than erosion. Despite this success, the predicted flat-to-ripple transition angle is off by about 20° because the set of crater functions used in that study are obtained from limited data of uncertain quality presented in two different sources, and an interpolation method is used to expand the data. Besides, the available crater functions only exist for incidence angles up to 67°, which limits the ability of the model to study pattern formation at high incidence angles. In order to overcome these limitations, this study uses MD simulations (using LAMMPS [24]) to obtain a set of crater functions for incidence angles up to 85°. Using this model, a systematic study was performed for silicon bombarded by Ar^+ ions of various energies (100 eV, 250 eV, 500 eV, 700 eV, and 1000 eV) at incidence angles of 0° to 80° to determine the role of mass redistribution and erosion for different incidence angles.

Furthermore, the model was used to study the pattern formation under simultaneous sample rotation and bombardment as well as under dual-beam bombardment, conditions that cannot be modeled by Norris's moment-based theory. Experimentally, these conditions are of great interest for creating novel nanostructures such as ordered dots on pure surfaces without impurity seeding [3,25–27]. However, modeling such systems with continuum theories is difficult, and efforts which have been made so far [28,29] have not shown satisfactory agreement with the experiments. Similarly, while kMC has been demonstrated as a useful alternative [30], the results obtained to date relied on a BH-like description of the surface and were unable to replicate the features obtained from experiments, although square ordering was observed. Thus, it was a good proof-of-concept test for the current model to investigate these novel experimental setups and compare the simulated and experimental results.

II. MODEL

A. Obtaining crater functions

The model considers each ion impact to result in a crater, which is understood to describe the *average* change in the local surface due to a single impact. The typical method of obtaining such a crater is to use MD to simulate many (typically 500–2000) single impacts at a prescribed incidence angle on a flat surface. Taking the average result of each MD impact and averaging the height change at each point relative to the impact location leads to the crater. In general, a crater has lateral and longitudinal extent of a few nanometers, results in subangstrom height changes over the affected area, and has a distinct pit-and-rim geometry. The use of MD craters is a key distinction between this and other models using kMC methods [15–18,31]. Although previous work has been done using craters obtained using a binary collision approximation model [20], the accuracy of those results could be questioned as the craters therein have extremely unrealistic vertical dimensions.

In this study, the Stillinger-Weber (SW) potential is employed to model interactions between silicon atoms since it has been tested in many MD simulations of ion bombardment and its reliability has been confirmed [32–36]. The parameters vary slightly from those given by Stillinger and Weber to better represent the amorphous phase [37]. The ion-silicon interactions are modeled by the ZBL universal potential proposed by Ziegler, Biersack, and Littmark [38]. For high-energy collisions, some silicon atoms can also come very close to each other, leading to the penetration of the atomic shells. In this case, the ZBL potential is also used for silicon-silicon interactions to include repulsive effects.

The amorphous silicon (a-Si) used in this work is prepared by the "melting-quenching" method in which crystalline silicon (c-Si) is melted and then quenched rapidly in a MD simulation [39–41]. The procedure is as follows:

(1) A silicon crystal consisting of $15 \times 10 \times 10$ lattices (with lattice length $a = 5.431$ Å) is created, resulting in a target with dimensions of 81.46 Å × 54.31 Å × 54.31 Å containing 12 000 atoms. With this size, the target can properly enclose the whole collision cascade produced by < 1 keV Ar^+ bombardment.

(2) Periodic boundary conditions (PBCs) are applied in all three directions. The target is heated up to 4000 K by velocity scaling. After being kept at 4000 K for 15 ps, the target is cooled down to 1 K by a cooling rate of 3.33×10^{13} K/s.

Another 15 ps is used to further equilibrate the target. The target is considered as an *NVT* ensemble and the time step is set to 0.5 fs.

(3) After completing step 2, a bulk a-Si target is created. This bulk a-Si target is then modified to become a surface by using a slab PBC configuration, i.e., a PBC is applied in the lateral directions (parallel to the surface, denoted as x and y axes) and no boundary condition in the direction of ions (normal to the surface, denoted as z axis). The bottom 5 Å of atoms are held fixed to prevent the target from moving. Due to the change of PBC and the creation of a surface, the target is no longer in the equilibrium state. To bring the target back to the stable state, the target is kept at 1 K using *NVT* integration until the potential energy ceases to increase.

For each ion impact, the a-Si target is configured as follows. The slab boundary conditions are used. The bottom 5Å of atoms are again held fixed to prevent the target from moving downwards under ion impacts. A layer with thickness of 1 nm is used as a thermostat layer that removes kinetic energies using a Berendsen thermostat [42] to keep the target temperature constantly at 1 K. The thermostat layer serves as a heat sink that mimics the bulk material. The free layer contains all the rest of the atoms above the thermostat layer. No thermostat is applied to the free layer. Atoms in the free layer are considered as an *NVE* ensemble. For each impact run, an ion is generated randomly above the surface with a specified incidence angle and azimuthal angle. The time step is chosen to be 0.1 fs to correctly simulate collisions between the high-velocity ion and target atoms. The collision cascade is allowed to fully develop for 11.4 ps. The whole target is then cooled down to 1 K to freeze the radiation damage for crater function calculation.

In order to investigate the effect of ion energy on surface evolution, simulations of Ar^+ ions with various energies (100, 250, 500, 700, and 1000 eV) on the a-Si target were performed. For each energy, 1000 or 2000 ion impacts were simulated at incidence angles from 0° to 85° with 5° increments to achieve good statistics.

B. kMC models

A slab boundary condition is applied to the target; i.e., periodic boundary conditions are used in the lateral directions (x and y direction) but not in the direction of the ion beam (z direction). The initial surface is randomly rough with an amplitude of one atomic spacing (about 0.27 nm for silicon).

The bombardment process begins as soon as the initial surface is set up. Ions are considered to generate inside a plane that is a few nanometers above the initial surface. Then, the ions progressively approach the surface until they collide with the target, in order to take shadowing effects into account. The height around the impact points is changed according to the crater function corresponding to the local incidence angle of each impact (i.e., the local slope).

In the present simulation, surface diffusion is treated discretely using an Arrhenius rate law in a manner similar to that of previous works [15,17]. The relative probability for an atom on the surface to undergo a diffusion event is given by the Arrhenius equation:

$$v = \left(\frac{2k_B T}{h}\right) \exp\left(-\frac{\Delta E}{k_B T}\right). \tag{1}$$

Here, T is the surface temperature, which is treated as a constant value over the entire surface and is taken as input. k_B and h are the Boltzmann and Planck constants, respectively. The principal variable under consideration here is the activation energy, ΔE, required to cause a hop.

There are several methods to determine the activation energy. A widely-used one is the net bond difference (NBD) method [15,17], which incorporates the net change in fulfilled bonds between the initial and final positions of a possible hop. The NBD method breaks down the activation energy into three components, given as

$$\Delta E = E_s + E_{nn} + E_{ES}. \tag{2}$$

Here, E_s is a substrate energy barrier present for all hops, representing the activation energy for a surface adatom. E_{nn} is the net bond breaking energy, based on the initial and final number of nearest neighbors for the given hop, such that

$$E_{nn} = \begin{cases} 0, & \text{if } nn_i \leqslant nn_f, \\ E_b(nn_i - nn_f), & \text{if } nn_i > nn_f. \end{cases} \tag{3}$$

Here, E_b is the neighbor bonding energy. Finally, the Ehrlich-Schwoebel barrier energy, E_{ES}, represents an additional energy barrier which applies only to hops which approach a step edge on the surface, but does not apply to atoms already on a step edge. The ES barrier inhibits atom diffusion over step edges, resulting in surface instability. However, step structures only exist on crystalline surfaces. On an amorphous surface, steps are nonexistent and so ES barriers are not considered.

The crater functions and kMC surface diffusion are coupled as follows: Ions arrive at the surface at regular time intervals based on the flux and simulated surface area. After each impact, the total hopping rate of all eligible surface atoms is updated, and an atom is selected to diffuse by treating its hopping rate as a relative event probability. After each diffusion event, a time step is computed based on the total surface hopping rate and the simulated time is incremented. Diffusion events continue to occur until the simulation time since the last ion impact is greater than or equal to the fixed time interval between impacts. This process allows the simulation to occur in "real" time, allowing atoms to make multiple hops in a short time frame. This is an improvement over prior approaches which used sweeps of the surface, as each surface atom could only execute one event (if any) in the entire time between such "sweeps."

It should be noted that while this method follows from previous kMC simulations, it may not be the most physically accurate representation of surface smoothening. In particular, it is generally accepted that an amorphous surface such as ion-bombarded Si undergoes primarily an ion-enhanced viscous flow type of relaxation. However, the current choice of model is sufficient to represent the phenomenon of surface smoothening and thus facilitate the study of crater functions as the primary pattern-forming mechanism, and the model itself is simple enough in concept to permit incorporation of a viscous flow component in later work.

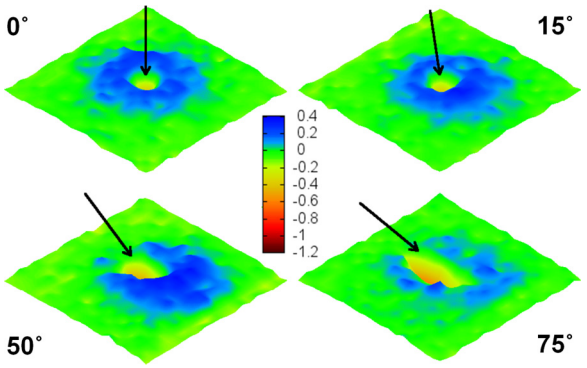

FIG. 2. (Color online) Sample craters for 500 eV Ar^+ on Si at various angles. Height scale units are angstroms. The black arrows indicate the direction of the ion beam. The size of each surface is 54.31 Å × 54.31 Å.

III. RESULTS AND DISCUSSION

A. Crater functions

For crater function calculation, the method proposed by Moseler *et al.* [43] is employed in this study. After each impact, the target is divided into a two-dimensional (2D) array of small vertical columns with a cross section of 2.71 Å × 2.71 Å. The height of each cell is determined by the highest atom in the corresponding column. In this way, the actual crater data from MD is used, as opposed to a functional fit such as the difference of Gaussians used in previous works [22,23].

Several sample craters are shown in Fig. 2 for 500 eV Ar^+ on Si at various angles. The craters are subangstrom in height. The key features are the central pit and the surrounding rim. At normal incidence, the crater is symmetrical, but as the incidence angle increases, the crater becomes more and more asymmetrical along the direction of the beam. The depth of the pit increases with increasing incidence angle up to 70° and then decreases with increasing angle above 70°. The pit is seen to elongate along the projected ion path as the impact angle increases. The rim is shown to maintain a largely consistent shape, but the center of the rim projects further along the projected ion path with increasing incidence angle.

B. Simulation results and phase diagram

A phase diagram is commonly used in materials science to describe distinct phases that occur at different conditions. In this work, a phase diagram is defined as a chart showing distinct types of pattern at different incidence angles and incident ion energies. A phase diagram of this type constructed from experimental data was shown by Madi *et al.* [10,11]. In order to compare with the experimental data, a similar phase diagram, shown in Fig. 3, was constructed from simulation results for ion energies of 100, 250, 500, 700, and 1000 eV for beam angles of 0°–80°. Unless stated otherwise, all simulations were run at a flux of 10^{15} cm^{-2} s^{-1}. Examples of different pattern types are given in Fig. 4. For all energies, the patterns are distinguished as the following types:

(1) flat surface for 0° to about 35°,
(2) transient ripples for 40° to 45°,
(3) well-aligned parallel-mode ripples for 45° to 70°,

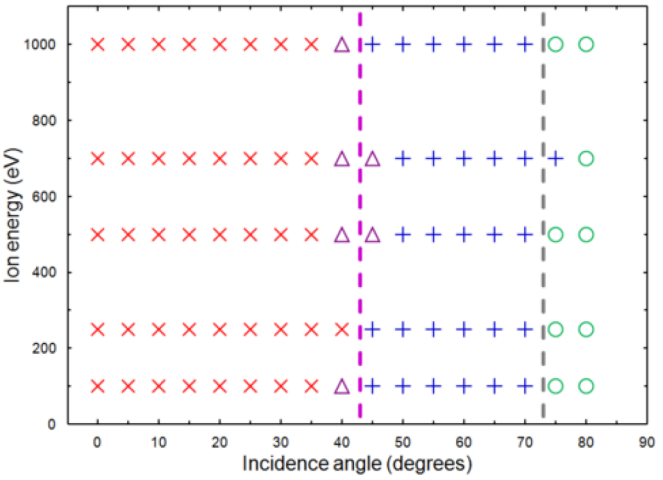

FIG. 3. (Color online) Phase diagram of various energies 100, 200, 500, 500, and 1000 eV. ×: flat; △: transient ripples; +: parallel-mode ripples; and ○: short-length stripes. The fluence is 2×10^{17} cm^{-2} in all cases. The dashed lines mark the transition angles.

(4) short-length stripes for 75° to 80°.

There are two transitions for the patterns. The first transition is at near 45° where the pattern changes from flat to parallel ripples. The other transition is at grazing incidence (about 75°) where the well-aligned ripples are replaced by irregular short-length stripes.

The phase diagram predicted by the MD/kMC simulations corroborates well with the experimental findings [10,44] that observed the flat-to-ripple transition at about 47°. However, the simulations did not predict the formation of perpendicular-mode ripples at glancing angles (>80°). This is most likely due to the low quality of crater functions above 80°. The crater functions are hard to obtain for high angles due to the difficulty of determining the impact points and the extremely high ion

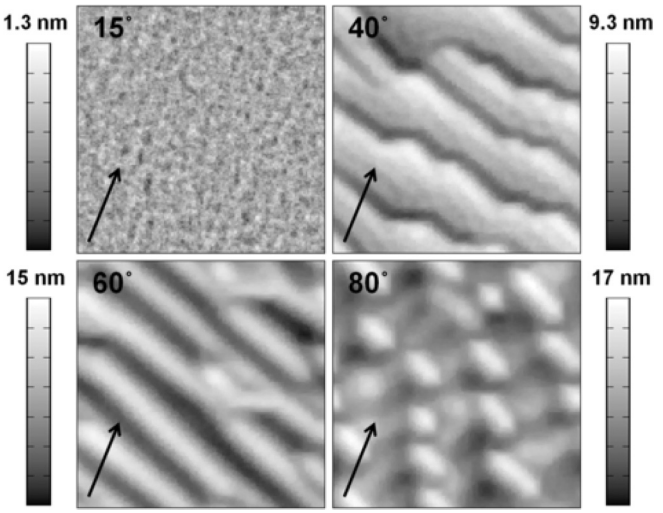

FIG. 4. Surface morphology of silicon bombarded by 500 eV Ar^+ at various incidence angles for a fluence of 2×10^{17} cm^{-2}. The beam direction is indicted by the arrow. The snapshots are 54.4 nm × 54.4 nm.

reflection rate (nearly 100% for >80°), leading to a low ratio of signal to noise. Even though the perpendicular mode was not predicted by the simulation, the formation of the irregular short-length stripes is a sign of transition. It is likely that with better-quality craters, proper perpendicular-mode ripples would be observable. Possible means for improving the craters are discussed in Sec. III F 2 below.

It should be mentioned briefly that for simulations performed with no diffusive component (achieved by setting the temperature to 0 K), the same qualitative trend was observed; i.e., the same phase diagram was observed. The qualitative aspects were different from the "with-diffusion" results in a manner consistent with expectations. That is, the wavelength was shorter and the amplitude much greater since there was no diffusive effect to moderate these characteristics. This is in agreement with conventional knowledge [1,8] that diffusion does not determine whether ripples will form but does affect the wavelength and amplitude of the ripples. Thus, it can be reasonably stated that the resulting patterns from the simulations arise due to the shape of the craters themselves, i.e., from the prompt redistribution and/or erosion of mass due to ion impacts.

To place this work in context, it is useful to compare the results obtained from the simulations with those obtained using the continuum theory developed by Norris *et al.* [8,45]. It should be emphasized that, although the results obtained using Norris's theory are calculated from the same MD data that is used in the kMC simulation, they are not reflective of the simulation methodology nor the validity of the simulated results, and the comparison is done only to place the work presented here in its larger context. The analytical form derived by Norris's theory is given by

$$\frac{\partial h(x,y,t)}{\partial t} = \left(S_x(\theta)\frac{\partial^2 h}{\partial x^2} + S_y(\theta)\frac{\partial^2 h}{\partial y^2}\right) - B\nabla^4 h, \quad (4)$$

where the coefficients are calculated by

$$S_x(\theta) = I_0 \frac{d}{d\theta}\left[M_x^{(1)}(\theta)\cos(\theta)\right], \quad (5a)$$

$$S_y(\theta) = I_0 M_x^{(1)}(\theta)\cos(\theta)\cot(\theta), \quad (5b)$$

where I_0 is the beam flux. The B parameter is the coefficient for the viscous flow. The viscous flow always relaxes the surface, thus the instability of the surface is determined by the curvature coefficients S_x and S_y. According to Eq. (5), the first moment of the crater functions is the key for S_x and S_y calculation. In the discrete system, the moments of the crater functions are calculated according to

$$M^{(0)} = \sum_{i=1}^{M}\sum_{j=1}^{N} \Delta h(i,j)\Delta x \Delta y = \Omega Y, \quad (6)$$

$$M_x^{(1)} = \sum_{i=1}^{M}\sum_{j=1}^{N} x_i \Delta h(i,j)\Delta x \Delta y, \quad (7)$$

$$M_y^{(1)} = \sum_{i=1}^{M}\sum_{j=1}^{N} y_j \Delta h(i,j)\Delta x \Delta y \cong 0, \quad (8)$$

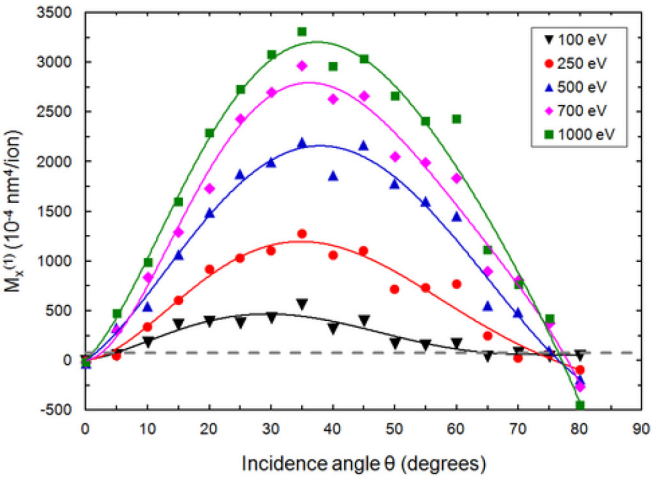

FIG. 5. (Color online) Calculated first moments of the craters about the x axis obtained for various energy and incidence angles. The fitted curves between data points are intended to guide the eye.

where $\Delta h(x,y)$ is the crater function; Δx and Δy are the side lengths of the small columns used in calculation of crater functions; M and N are the number of columns on the x side and y side, respectively (note that $i \neq x$ and $j \neq y$); $M_x^{(0)}$ is the zero moment and is simply the sputtering yield per ion in volume units. $M_x^{(1)}$ and $M_y^{(1)}$ are the x and y components of the first moment that describes the magnitude and direction of the net mass movement. Figure 5 displays the $M_x^{(1)}$ calculated for the crater functions obtained in this work. The y-component moments are not shown here because they are nearly zero due to axisymmetry.

As shown in Fig. 5, the moment is nearly zero at 0° due to symmetry. The moment becomes positive at off-normal angles due to the asymmetry of the craters. The moment is the summation of the positive contribution from the rim and the negative contribution from the pit. As long as the contribution from the rim is greater than from the pit, the moment is positive. The moment increases with increasing incidence angle until a maxima is reached at about 40°. After 40°, the moment decreases with the angle due to the elongation of the craters and particularly the pits. At 80°, the contribution of the pit exceeds the rim, leading to a negative moment, which indicates that the pit contribution is dominant. The moment varies approximately linearly with the ion energy, since higher energies induce larger craters.

As discussed above, the signs of the curvature coefficients S_x and S_y determine the ripple formation and orientation. Thus, to compare the simulated results with those expected from the continuum model, the curvature coefficients were calculated and are shown in Fig. 6 for the 500 eV test case. If $S_x > 0$ and $S_y > 0$, the surface remains flat. If $S_x < 0$ and $S_y > 0$, parallel-mode ripples will form assuming the beam is parallel to the x axis. If $S_x > 0$ and $S_y < 0$, perpendicular-mode ripples will form. If both S_x and S_y are negative, ripples will form with orientation determined by $\max(|S_x|,|S_y|)$. From inspection of Fig. 6, the phase behavior of the ripples can be estimated based on these criteria.

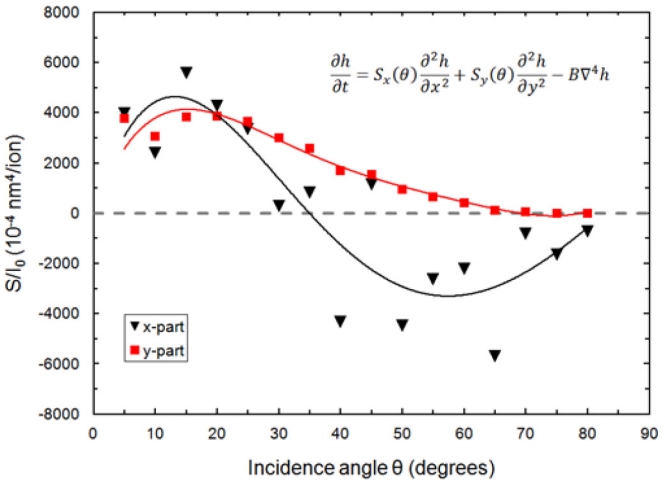

FIG. 6. (Color online) Calculated curvature coefficients for 500 eV Ar^+ on Si, according to the formulas by Norris as given in the main text. According to linear theory, the surface is flat if both coefficients are positive, and instability occurs if one or both are negative, with the more negative of the pair determining the pattern orientation. Note that, although the data shown here result from calculations performed with the same crater data as used in the kMC simulations, these data are not necessarily indicative of the simulation results. The fitted curves are to guide the eye.

The phase diagram predicted by the moment description of analytical equations is summarized in Table I. The moment criterion predicts a flat-to-ripple transition, in agreement with the simulated and experimental results. However, the transition angle is found to be only about 35°, which is notably lower than the value obtained from the simulation results and that found in experiments, although it could be pointed out that the transition point is rather uncertain from the data shown. Similar data for the other ion energies shows the same trend.

To explain this discrepancy, it is worth noting that recent work [12] has shown that the simple moment-based expressions given above cannot represent experimental data, regardless of the values of the moments themselves. Further efforts have shown [13] that this may be due to an incomplete mathematical formulation, and that incorporating surface curvature into the derivation of the coefficients may resolve the mathematical issues. Since the simulation uses the craters directly to model the surface evolution, it is not necessary to compute moments or curvature coefficients, and thus the limitations of the continuum theory discussed above do not apply (although the craters do have some weaknesses, which are discussed in Sec. III F below). This is a likely explanation for why the simulation results shown in Fig. 3 show better

TABLE I. Phase behavior predicted by the moment of the crater function

Incidence angle	S_x	S_y	Predicted pattern
0°–35°	>0	>0	Flat, stable surface
35°–77°	<0	>0	Parallel-mode ripples
77°–80°	<0	<0	Mixed-mode ripples

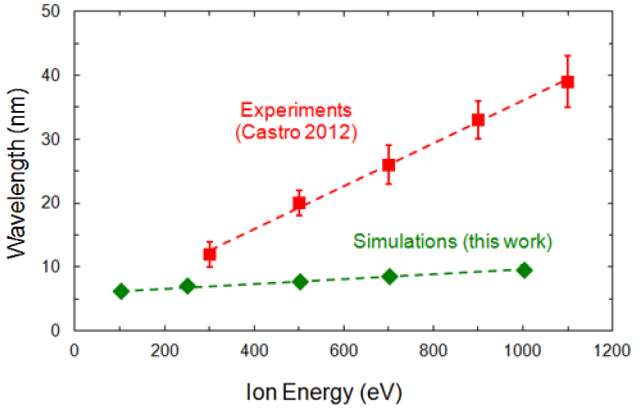

FIG. 7. (Color online) Plot of the simulated ripple wavelengths with respect to the incident ion energy at fixed incidence angle (60°), showing weakly linear scaling behavior in qualitative agreement with experimental observations at 65° by Castro *et al.* [44].

experimental agreement than the results from the continuum model.

Even though the simulation results agree with experimental results in terms of the phase diagram, the wavelengths of ripples are not predicted correctly. The wavelengths of the simulated ripples were plotted against the incident ion energy in Fig. 7. In the figure, the simulated results show a weakly linear relationship between wavelength and energy. The qualitative trend is in agreement with experimental observations [44]. However, the exact values of the wavelengths as well as the rate of growth with increasing energy are significantly less than the experimental data. This can be attributed to weaknesses in the choice of diffusion model, as discussed below in Sec. III F. Thus, although the qualitative trends from the simulated results are encouraging, future work is needed to improve the smoothening mechanism to obtain better quantitative results. In contrast, the linear dependence of the wavelength with the ion energy is correctly reproduced by the "hydrodynamic" models in which the relaxation of the amorphous layer is assumed to be driven by stress [46]. Thus, including the effects of ion-induced stress is a possible improvement in this respect.

C. Role of erosion effects

Previous works using crater functions [8,9,22,23,43,45] have demonstrated that erosion is essentially negligible or even irrelevant at least for low and intermediate angles. On the other hand, many works such as the classic Bradley-Harper theory [1] attribute erosion as the dominant force in pattern formation. Since the craters contain both erosive and redistributive elements, simulations were conducted using erosion-only crater functions in order to separate the two effects. In the same way that the above results are in parallel with the continuum theory of Norris, the results presented here can be considered as parallel to the Bradley-Harper model, and the comparison between redistributive and erosive elements given here is analogous to a comparison between these two descriptions.

The crater functions obtained in the previous section are the summation of the erosive and the redistributive contributions. In order to separate these two effects, the erosive crater

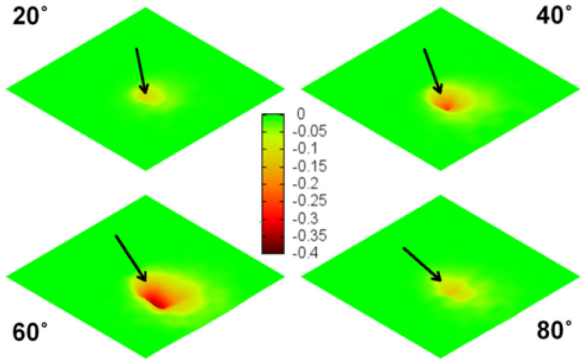

FIG. 8. (Color online) Examples of erosive crater functions for 500 eV Ar+ on Si at various angles. Height scale units are in angstroms. The black arrows indicate the direction of the ion beam. The size of each surface is 54.31 Å × 54.31 Å.

functions were obtained in a similar manner as the composite crater functions. For every impact, the height of the location where the sputtered atom(s) originated was reduced. By averaging over 1000 impacts, the erosive crater functions were obtained. A few examples are shown in Fig. 8 for 20°, 40°, 60°, and 80°. As expected, an erosive crater only contains a hole which increases in size as the incidence angle increases until about 65°, following the trend of the angle-dependent sputtering yield. The hole also becomes elongated as the angle increases, similar to the holes of the composite craters.

With other simulation parameters the same as in the previous section, the surface evolution was simulated using the erosive crater functions. The resulting topographies can be distinguished as follows, as shown in Fig. 9:

(1) at 0°, the surface is almost flat;

(2) from 5° to 30°, the surface appears as randomly arranged holes;

(3) from 35° to 50°, irregular short-length perpendicular-mode ripples;

(4) from 55° to 85°, well-aligned perpendicular-mode ripples.

It is important to note that the results given here are not, strictly speaking, physical since these craters do not show all the effects of ion impacts as before, but instead show only the erosive effects. However, these results can be considered as prototypical of those expected from a generic erosion-dominated system where erosive components are dominant over redistributive components (such as might be seen for high-energy bombardment, where the sputtering yield is much larger [20]). Thus, in a system where the surface features shown here are observed, it can be concluded that erosion is the dominant physical mechanism, as with the perpendicular-mode ripples for glancing angles. Conversely, since the features obtained here do not match with, e.g., the parallel-mode ripples observed for intermediate incidence in Fig. 3, these results lend further support to the conclusion that redistribution is dominant in those regimes where such patterns are observed, since erosion alone is unable to reproduce those results.

In order to understand the origin of these patterns, the moment of the erosive component together with that of the redistributive component and their total were calculated, as shown in Fig. 10. In general, the magnitude of the moment due to a mechanism is roughly equivalent to the magnitude of the effect from that mechanism. The magnitude of the erosive moment is at least an order of magnitude smaller than the redistributive moment for most angles, but their magnitudes are comparable at high angles (>70°). This implies that the redistributive effects are dominant at low and intermediate angles, while erosive effects become significant at high angles.

To better associate the moment with pattern type, the curvature coefficients S_x and S_y contributed from erosive moments are displayed in Fig. 11. S_y is negative for all angles, which implies that the surface is destabilized at all angles. S_x has a turning point at 65° where its sign is changed. S_x and S_y are comparable for angles <15°, which may explain the formation of holes. $|S_x| > |S_y|$ for 20°–60°, suggesting that

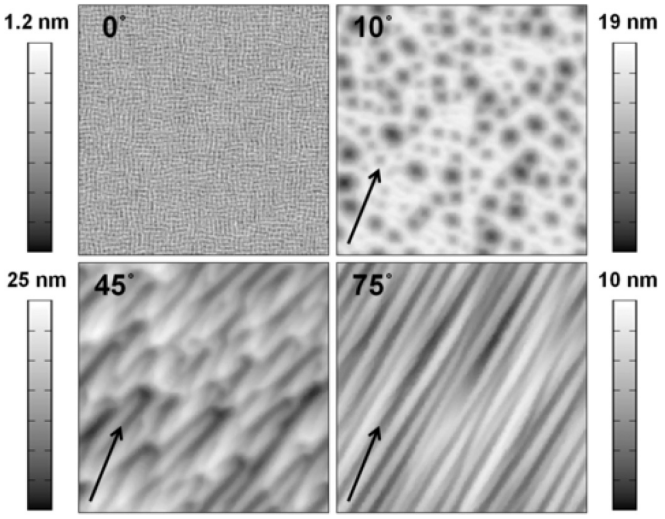

FIG. 9. Examples of simulation results using erosion-only crater functions. The beam direction is indicated by the arrow. All snapshots are 108 nm × 108 nm and the fluence in each case is 10^{16} cm^{-2}.

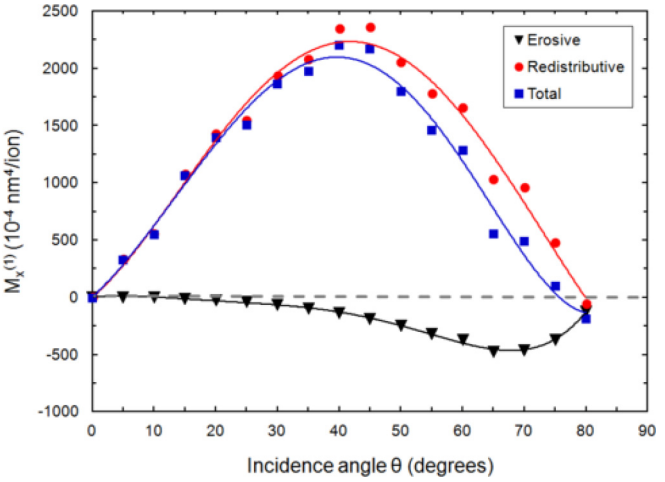

FIG. 10. (Color online) The first moments of the erosive component, the redistributive component, and their total of the craters for 500 eV Ar^+ on Si at various incidence angles. The fitted curves are to guide the eye.

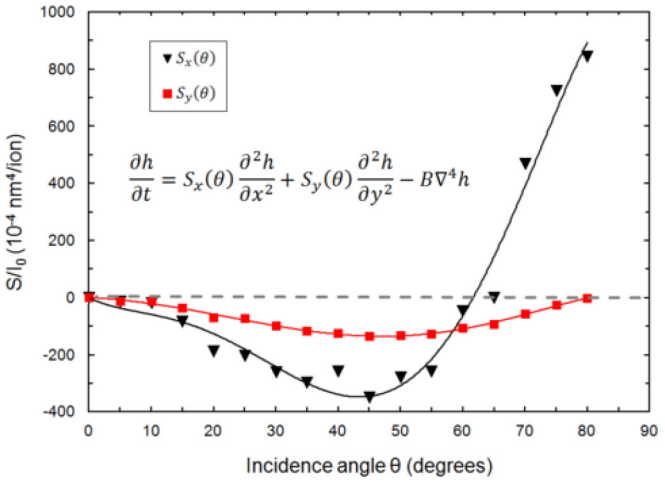

FIG. 11. (Color online) The contributions to the continuum theory curvature coefficients, S_x and S_y, from erosion. The data are taken from 500 eV Ar^+ incident on Si at various angles. The fitted curves are to guide the eye.

parallel-mode ripples should form. This is not in agreement with the simulation results. S_x becomes positive for angles $>65^\circ$, indicating the formation of perpendicular mode ripples, which agrees with the simulation results.

Although the agreement between the moment analysis and the simulation results is not exact, a key conclusion can still be drawn based on several observations. First, erosion is irrelevant for lower angles as its contribution is dominated by the redistributive contribution. Conversely, erosion is significant at high angles where the redistributive moment is fairly small. From the simulation results, it appears that the primary pattern that can be formed from erosion is the perpendicular-mode ripples. Thus, it can be concluded erosion does not contribute to the formation of parallel-mode ripples, but contributes significantly to the development of perpendicular-mode ripples. Although this conclusion is difficult to verify by experiments (as the two mechanisms cannot be separated so conveniently), it does agree with previous theoretical work for low-energy ion irradiation, e.g. [20], despite using a different approach to describe the surface evolution.

D. Pattern formation on rotated samples

Irradiating a substrate during simultaneous substrate rotation can generate unique patterns, including quantum dots and curved ripples [5]. In particular, much interest has been focused on the formation of nanodots on pure surfaces such as Si without relying on undesirable metal impurities [5,27]. Unfortunately, theoretical efforts are not quite as advanced as the experimental interest. Continuum approaches currently rely on assuming a uniform distribution of azimuthal angles corresponding to the limit of high rotation frequency [47], and thus are not useful for studying the effects of varying frequencies. While the kMC approach is able to consider frequency regimes [19,30], the structures obtained thus far show poor resemblance to those obtained in experiment, as the results were disordered holes rather than ordered dots. With this in mind, a study of patterning on rotated samples

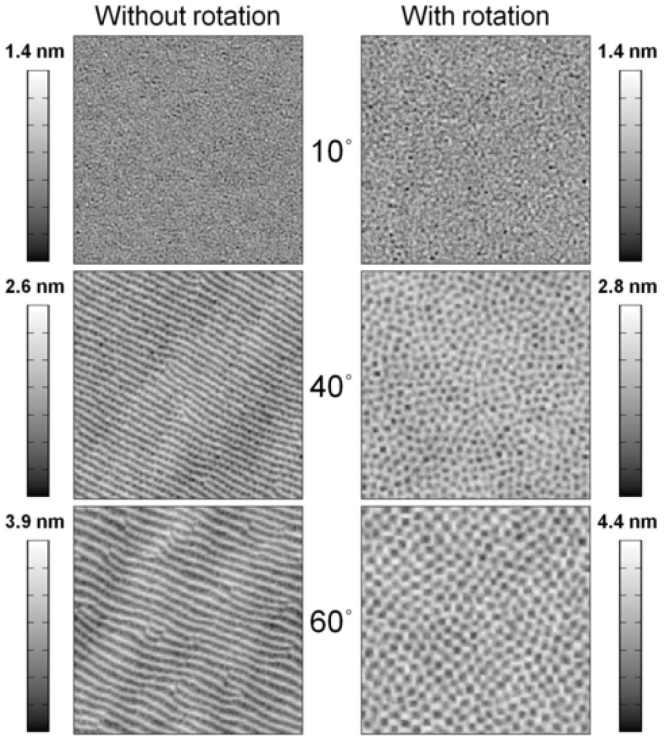

FIG. 12. Comparison of patterns with and without rotation at 10°, 40°, and 60° with a fixed rotation speed of 1.257 rad/s. The size of each image is 70 nm × 70 nm, and the fluence in each case is 10^{17} cm^{-2}.

was conducted using the present model to determine if some improvement in the results could be obtained.

To carry out this study, the sample rotation was modeled by changing the azimuthal angle based on a given rotation rate. The simulations were performed for 500 eV Ar^+ at various incidence angles and different rotation speeds. Figure 12 gives the comparison of patterns with and without rotation at 10°, 40°, and 60° incidence with a fixed rotation speed of 1.257 rad/s (12 rpm). Arrays of square-ordered dots are formed for 40° and 60° incidence with rotation. Although the dots were not as well defined as in the experimental results, the overall quality and square ordering was an improvement over previous kMC work in this area. The patterns generated with sample rotation are strongly related to patterns obtained without rotation. If ripples are not formed without rotation, then the surface remains flat with rotation as the 10° case. The size and the spacing of the dots also scale linearly with the wavelength of the ripples formed without rotation.

Square-ordered dots are not always formed. Figure 13 shows the surface profile at different fluences for 60° incidence with a rotation speed of 0.126 rad/s (1.2 rpm), or 10 times slower than previous value. Disordered ripples formed instead of dots. Interestingly, the ripple orientation also rotates as the sample rotates. This can be interpreted as follows: when the rotation speed is very slow, the azimuthal angle can be seen as almost constant for a period of time. During this period, the ripple can form. Then, as the azimuthal angle slowly changes, the ripples are essentially destroyed and recreated by the ion beam, never achieving long-range order.

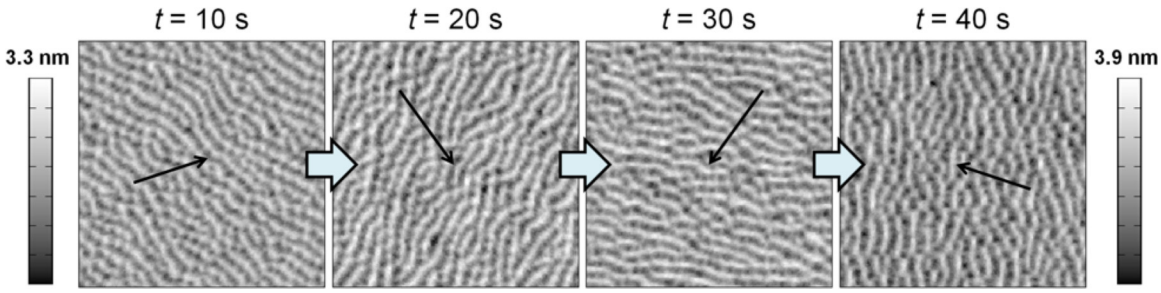

FIG. 13. (Color online) Surface profiles at different irradiation times at 60° incidence with a rotation speed of 0.126 rad/s. The size of each image is 70 nm × 70 nm. The arrows indicate the direction of the ion beam at the time each snapshot was obtained.

Thus, a key result from these studies is that there exists a critical value for the rotation speed, such that when the rotation speed is larger than this critical value, square-ordered dots are formed. Increasing the speed does not improve the ordering of the dots. When the speed is smaller than the critical value, rotating ripples are formed. This critical rotation speed was found to be around 0.5 rad/s (5 rpm). This rotation-rate dependence cannot be replicated by linear continuum models, which are restricted to the regime of arbitrarily fast rotation.

E. Dual-beam bombardment

Experimental studies by Joe *et al.* have shown that ordered dots or modulated ripples can be generated by bombardment of a Au target using two beams that are perpendicular to each other [25,26]. In their analysis, the experimenters noted that existing continuum theories were inadequate for describing the behavior of the surface under dual-beam irradiation. Similarly, previous kMC results [30] demonstrated the square-ordered surface, but predicted holes instead of dots and were not able to show the modulation of the ripples for unbalanced beams.

In order to further demonstrate improvement over the previous results, then, simulations were conducted for dual beams arranged at a 90° azimuthal separation. Since the model is designed to mimic bombardment processes, it can reproduce dual-beam sputtering easily. Pattern formation was studied on a simulated Si target under 500 eV dual Ar^+ beams for a flux of 10^{15} cm^{-2} s^{-1} and fluences up to 5×10^{16} cm^{-2}.

The model demonstrates the unique ability to reproduce pattern formation under these irradiation conditions. In Fig. 14, the resulting surface profiles are shown for different incidence angles when both beams have the same flux. When compared to Fig. 4, it can be found that the patterns generated by dual-beam sputtering are strongly correlated with single-beam sputtering. At 0° to 35°, the surface remains flat, acting the same way as single-beam sputtering. Starting from 40° where ripples start to form for single-beam sputtering, ordered dots begin to appear. At 60°, the dots are well defined, corresponding to the well-formed ripples for single-beam bombardment at these incidence angles. The dots become sparse at 80°, which may be related to the short ripples for single-beam sputtering. In any case, it is clear that these results show significant improvement over previous modeling efforts in this area.

By changing the flux ratio of the two beams, a new set of patterns can be created. Figure 15 gives the surface profile of Si under 500 eV dual Ar^+ beams with different fluxes at

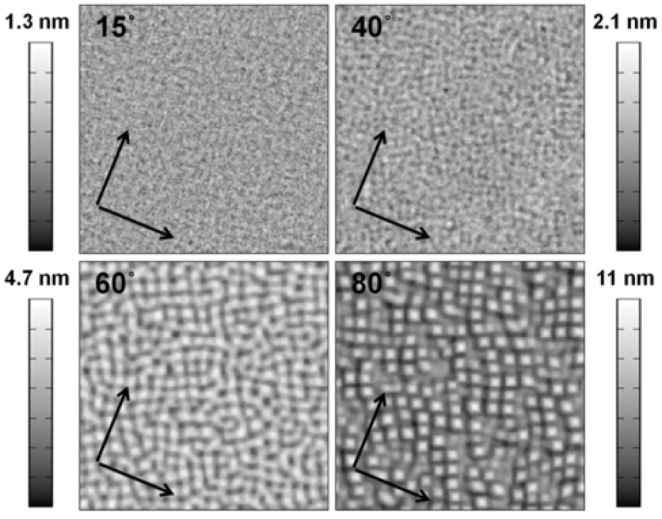

FIG. 14. Surface profiles of Si under 500 eV Ar^+ dual-beam sputtering at various incidence angles. The arrows indicate the beam directions projected on the surface. Each snapshot is 108 nm × 108 nm and the fluence in each case is 2.5×10^{16} cm^{-2}.

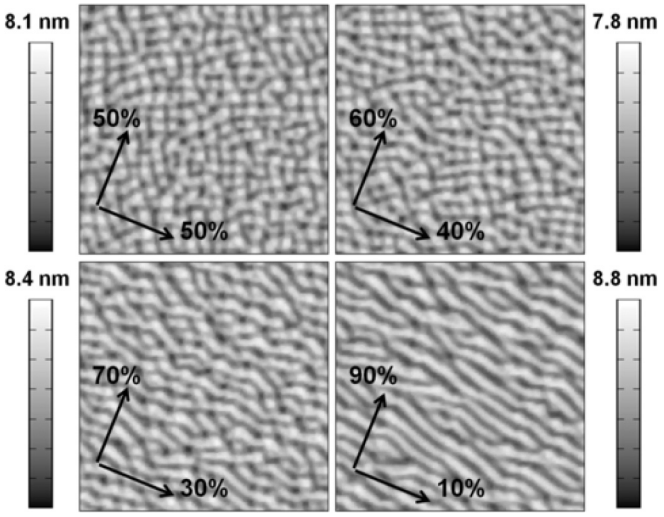

FIG. 15. Various patterns formed under different flux ratios of the two beams, both incident at 65°. Each surface is 108 nm × 108 nm. The arrows indicate the beam directions projected on the surface, and the percentages represent the relative fluxes of the two beams as a fraction of the total flux, which is 10^{15} cm^{-2}.

60° incidence. Using equal fluxes for the two beams, only dot structures are generated. If the fluxes become unequal for the beams, the surface patterns differ from a mixture of dots and ripples (60% of total flux from beam 1), to dots fused with ripples (70%, 80% from beam 1), and eventually to ripple-only structures (90%, 100% from beam 1). These simulation results are again similar to the experimental results of Joe *et al.*, although the substrate materials are different.

F. Shortcomings of the current model

1. Shortcomings of the current diffusion model and effects of relaxation mechanisms

Although the simulation results corroborate well with the experimental findings for many features of the surface evolution, the ripple wavelength and amplitude are predicted incorrectly. The wavelength predicted by the simulations is about 3–4 times smaller than the experimental observations. On the other hand, the amplitude is overestimated by about 50% on average. Such mismatches pose concerns about the validity of the kMC diffusion model. Thus, it is necessary to inspect the possible reasons for such mismatches and their effects on surface evolution.

The issue of incorrect wavelength and amplitude is common in models that employ a kMC diffusion approach [15,17]. To see why this is, begin by inspecting Eq. (4), reprinted below:

$$\frac{\partial h(x,y,t)}{\partial t} = \left[S_x(\theta)\frac{\partial^2 h}{\partial x^2} + S_y(\theta)\frac{\partial^2 h}{\partial y^2} \right] - B\nabla^4 h. \quad (4)$$

The rightmost term ("B term") represents the diffusive force which serves to mediate the pattern characteristics, as first discussed by Bradley and Harper [1]. The short wavelength and high amplitude observed in kMC simulations are an indication of a weak smoothing force. In other words, the B term in the continuum theory is underestimated by the simulations compared to its real value. However, the underestimation of the B term does not impair kMC studies of pattern formation, because it is the mass redistribution and/or erosion that determines the pattern types, as demonstrated in both the curvature-dependent sputtering and moment-description formalisms [1,8]. The diffusion process only mediates the surface roughness to determine the resulting wavelength and amplitude. As mentioned above (Sec. III B), simulations were carried out with no active diffusion by setting the temperature to zero over the same parameter space (0°–80° and 100–1000 eV incidence). The simulations yielded the same phase diagram as the one with diffusion, except with unrealistic ripple wavelengths and amplitudes. Thus, as long as the simulations are able to study different effects on pattern formation, the underestimation of the B term does not make the simulations invalid. However, it does prohibit accurate output of wavelength, amplitude, and saturation fluence information from the simulations.

The underestimation of the smoothing force could be for several reasons. One is the relatively high value of binding energy E_{nn} used in the calculation of the activation energy. The binding energy determines the probability for an atom to reduce its coordination number. With the binding energy used in this work, almost all (>99.99%) of the diffusion flux is composed of point defect (adatom/vacancy) motion or edge diffusion. Consequently, once an atom binds to another atom or a cluster, it is almost impossible for the bond to break. This effect dramatically reduces the downhill current that relaxes the surface. Using a lower binding energy is an option to tackle this issue [15,17], but it may render the simulation unphysical if not done carefully.

The second reason is that surface diffusion may not be the dominant driving mechanism for relaxation, as alluded to previously. It is known that an amorphous layer is formed when a semiconductor is under ion irradiation. The irradiation-enhanced viscous flow of this layer is considered to be the dominant smoothing mechanism as opposed to thermally activated surface diffusion near room temperature [48,49]. However, viscous flow is difficult to model atomistically, so including it would necessitate the use of alternative methods [22].

2. Shortcomings of the crater functions

Although the model presented here is not subject to nearly as many problems as the moment-based continuum theory, as discussed above, the crater function approach is not without flaws. Arguably the most significant flaw is that, for the current method for obtaining craters, the determination of the impact location is too simplistic. Currently, the initial ion trajectory is simply projected onto the surface to determine the impact location. However, in reality as the ion approaches the surface it will interact with the surface atoms, leading to some degree of repulsion which may push the impact point forward of its projected location or even reflect the ion before it collides in the surface at all. This effect would be most noticeable at the highest angles, and is probably a significant part of the reason why the current high-angle craters and simulation results are of relatively poor quality compared to the rest. In addition to improving the high-angle craters, improving the impact point calculation would also tend to negatively shift the crater moments at higher angles, allowing clear prediction of a perpendicular-mode transition if the continuum model is applied.

Another possible weakness of the current craters is the neglect of surface curvature [13]. It was shown in this work that the surface instability may be partially influenced by the curvature dependence of the craters. Comparison of the simulated results to experiments might suggest that this effect is not critical over most angles, since good agreement is obtained for the flat-to-rippled transition. However, this effect may be quite prominent at the highest angles, since the parallel-to-perpendicular transition has been shown to be dominated by erosive mechanisms, which are well known to be strongly dependent on surface curvature [1]. That said, since the simulated results for erosion-only craters already show formation of perpendicular-mode ripples in the high-angle regime without any explicit curvature dependence, the importance of curvature even at these angles remains the subject of future studies. Furthermore, although Nietiadi and Urbassek have shown that surface curvature has a significant effect on the shape of the crater function [50], their results were obtained on surfaces with very small radii of curvature, so the observed effects would be significantly less dramatic in a more realistic system.

As a final note, it is worth mentioning that pattern formation on ion-bombarded amorphous surfaces has in recent years been described by an alternative "hydrodynamic" theory [46]. In theory, the craters themselves could contain most of the prompt/local effects of the ion impact, while switching to a viscous flow model of smoothening would contain the longer-term effects. However, the effects of stress in the amorphous layer, which have drawn much attention recently, may not be adequately considered by the current kMC model. In this case, future work may be necessary to determine how best to treat the stress physics of the surface using the MD crater data, possibly deriving some form of stress distribution from the MD simulations.

IV. CONCLUSIONS AND FUTURE WORK

The hybrid MD/kMC atomistic model developed in this work has been demonstrated to be a powerful tool for studying surface evolution under ion bombardment. Unlike the continuum theory, this model is atomistic and thus is designed in a way that mimics a real bombardment experiment. Ion impacts are treated stochastically using crater functions to model the resulting surface height changes due to each impact. The smoothing process is modeled using a kMC Arrhenius diffusion as done in previous studies.

The systematic study conducted using this model has shown that erosion is irrelevant at low incidence angles and negligible at intermediate angles in the pattern formation. However, the results of erosion-only simulations neglecting any redistributive effects have shown that erosion plays the dominant role in perpendicular-mode ripple formation at glancing angles, which has not been shown previously by models using crater functions based on MD simulations.

Additionally, the model also has the unique ability to simulate complex experimental setups, such as sample rotation or dual-beam bombardment, while obtaining superior results compared to previous efforts. For sample rotation, a critical rotation speed was found ($\sim$0.5 rad/s or 5 rpm) below which only disordered ripples would form, but above which squared-ordered dots were observed. For dual-beam sputtering, the pattern formation was found to correlate with the patterns obtained under single-beam sputtering, and while square-ordered dots were achieved for higher angles, increasing the flux of one beam relative to the other resulted in mixed dot-ripple structures similar to the modulated ripples observed experimentally.

For future work, efforts should be devoted to addressing the issue of incorrect prediction of wavelength and amplitude. Incorporating viscous flow is a possible solution. However, since viscous flow is difficult to model atomistically, it is best treated by an approach like that used in the work by Kalyanasundaram *et al.* [22].

Establishing a reliable way to obtain crater functions at glancing angles is also crucial. In this work, the crater obtained at 85° was dominated by random noise. This is believed to be caused by an oversimplified method for determining the impact point. At glancing angles the effects of surface-ion repulsion and small surface roughness variations are significant and must be accounted for in a revised methodology. Additionally, the current crater functions are all obtained for flat surfaces. However, the surface curvature may affect the crater function. Thus, it is worthwhile to obtain crater functions for different surface curvatures and investigate their effect on the resulting morphology.

ACKNOWLEDGMENTS

This work was supported by the U.S. Department of Energy under the Grant No. DE-SC-0010719. M.L. was supported by the National Science Foundation Graduate Research Fellowship under Grant No. DGE-1144245. Any opinion, findings, and conclusions or recommendations expressed in this material are those of the authors(s) and do not necessarily reflect the views of the National Science Foundation.

[1] R. M. Bradley and J. M. E. Harper, Theory of ripple topography induced by ion bombardment, J. Vac. Sci. Technol. A **6**, 2390 (1988).

[2] S. Facsko, T. Dekorsy, C. Koerdt, C. Trappe, H. Kurz, A. Vogt, and H. Hartnagel, Formation of ordered nanoscale semiconductor dots by ion sputtering, Science **285**, 1551 (1999).

[3] F. Frost, A. Schindler, and F. Bigl, Roughness evolution of ion sputtered rotating inp surfaces: Pattern formation and scaling laws, Phys. Rev. Lett. **85**, 4116 (2000).

[4] M. Makeev, R. Cuerno, and A. Barabasi, Morphology of ion-sputtered surfaces, Nucl. Instrum. Methods Phys. Res., Sect. B **197**, 185 (2002).

[5] F. Frost, B. Ziberi, A. Schindler, and B. Rauschenbach, Surface engineering with ion beams: From self-organized nanostructures to ultrasmooth surfaces, Appl. Phys. A **91**, 551 (2008).

[6] W. L. Chan and E. Chason, Making waves: Kinetic processes controlling surface evolution during low-energy ion sputtering, J. Appl. Phys. **101**, 121301 (2007).

[7] J. Muñoz-García, R. Cuerno, and M. Castro, Coupling of morphology to surface transport in ion-beam-irradiated surfaces: Normal incidence and rotating targets, J. Phys. Condens. Matter **21**, 224020 (2009).

[8] S. Norris, J. Samela, L. Bukonte, M. Backman, F. Djurabekova, K. Nordlund, C. Madi, M. Brenner, and M. Aziz, Molecular dynamics of single-particle impacts predicts phase diagrams for large-scale pattern formation, Nat. Commun. **2**, 276 (2011).

[9] M. Z. Hossain, K. Das, J. B. Freund, and H. T. Johnson, Ion impact crater asymmetry determines surface ripple orientation, Appl. Phys. Lett. **99**, 151913 (2011).

[10] C. Madi, H. Bola George, and M. Aziz, Linear stability and instability patterns in ion-sputtered silicon, J. Phys. Condens. Matter **21**, 224010 (2009).

[11] C. S. Madi and M. J. Aziz, Multiple scattering causes the low energy–low angle constant wavelength topographical instability of argon ion bombarded silicon surfaces, Appl. Surf. Sci. **258**, 4112 (2012).

[12] J. C. Perkinson, E. Anzenberg, M. J. Aziz, and K. F. Ludwig, Model-independent test of the truncated crater function theory of surface morphology evolution during ion bombardment, Phys. Rev. B **89**, 115433 (2014).

[13] M. P. Harrison and R. M. Bradley, Crater function approach to ion-induced nanoscale pattern formation: Craters for flat surfaces are insufficient, Phys. Rev. B **89**, 245401 (2014).
[14] A. Hartmann, R. Kree, U. Geyer, and M. Kölbel, Long-time effects in a simulation model of sputter erosion, Phys. Rev. B **65**, 193403 (2002).
[15] E. Chason, W. Chan, and M. Bharathi, Kinetic Monte Carlo simulations of ion-induced ripple formation: Dependence on flux, temperature, and defect concentration in the linear regime, Phys. Rev. B **74**, 224103 (2006).
[16] B. Liedke, K.-H. Heinig, and W. Moller, Surface morphology and interface chemistry under ion irradiation—simultaneous atomistic simulation of collisional and thermal kinetics, Nucl. Instrum. Methods Phys. Res., Sect. B **316**, 56 (2013).
[17] A. Hartmann, R. Kree, and T. Yasseri, Simulating discrete models of pattern formation by ion beam sputtering, J. Phys. Condens. Matter **21**, 224015 (2009).
[18] B. Liedke, Ion beam processing of surfaces and interfaces—modeling and atomistic simulations, Ph.D. thesis, Helmholtz-Zentrum Dresden-Rossendorf, 2011.
[19] I. Koponen, O. P. Sievänen, M. Hautala, and M. Hakovirta, Simulations of sputtering-induced roughening and formation of surface topography in deposition of amorphous diamond films with mass-separated kilo–electron volt ion beams, J. Appl. Phys. **82**, 6047 (1997).
[20] H. Hofsäss, Surface instability and pattern formation by ion-induced erosion and mass redistribution, Appl. Phys. A **114**, 401 (2014).
[21] W. Moller, TRI3DYN—Collisional computer simulation of the dynamic evolution of 3-dimensional nanostructures under ion irradiation, Nucl. Instrum. Methods Phys. Res., Sect. B **322**, 23 (2014).
[22] N. Kalyanasundaram, J. B. Freund, and H. T. Johnson, A multiscale crater function model for ion-induced pattern formation in silicon, J. Phys. Condens. Matter **21**, 224018 (2009).
[23] Z. Yang, M. Lively, and J. P. Allain, Atomistic simulation of ion beam patterning with crater functions, Nucl. Instrum. Methods Phys. Res., Sect. B **307**, 189 (2013).
[24] S. Plimpton, Fast parallel algorithms for short-range molecular dynamics, J. Comput. Phys. **117**, 1 (1995).
[25] M. Joe, C. Choi, B. Kahng, and J.-S. Kim, Nanopatterning by dual-ion-beam sputtering, Appl. Phys. Lett. **91**, 233115 (2007).
[26] M. Joe, J.-H. Kim, C. Choi, B. Kahng, and J.-S. Kim, Nanopatterning by multiple-ion-beam sputtering, J. Phys. Condens. Matter **21**, 224011 (2009).
[27] D. Chowdhury, D. Ghose, and B. Satpati, Production of ordered and pure Si nanodots at grazing ion beam sputtering under concurrent substrate rotation, Mater. Sci. Eng. B **179**, 1 (2014).
[28] S. Vogel and S. J. Linz, Surface structuring by multiple ion beams, Phys. Rev. B **75**, 085425 (2007).
[29] M. Joe, C. Choi, B. Kahng, C. Kwak, and J.-S. Kim, Patterning by ion-beam sputtering, J. Korean Phys. Soc. **52**, 181 (2008).
[30] T. Yasseri and R. Kree, A Monte Carlo study of surface sputtering by dual and rotated ion beams, Nucl. Instrum. Methods Phys. Res., Sect. B **268**, 2496 (2010).
[31] I. Koponen, M. Hautala, and O. P. Sievänen, Simulations of ripple formation on ion-bombarded solid surfaces, Phys. Rev. Lett. **78**, 2612 (1997).
[32] T. Diaz de la Rubia and G. Gilmer, Structural transformations and defect production in ion-implanted silicon: A molecular dynamics simulation study, Phys. Rev. Lett. **74**, 2507 (1995).
[33] L. A. Marqués, M. J. Caturla, T. Díaz de La Rubia, and G. H. Gilmer, Ion beam induced recrystallization of amorphous silicon: A molecular dynamics study, J. Appl. Phys. **80**, 6160 (1996).
[34] M.-J. Caturla, T. Díaz de la Rubia, L. Marqués, and G. Gilmer, Ion-beam processing of silicon at keV energies: A molecular-dynamics study, Phys. Rev. B **54**, 16683 (1996).
[35] K. Nordlund, M. Ghaly, R. Averback, M. Caturla, T. Diaz de la Rubia, and J. Tarus, Defect production in collision cascades in elemental semiconductors and fcc metals, Phys. Rev. B **57**, 7556 (1998).
[36] N. Kalyanasundaram, M. C. Moore, J. B. Freund, and H. T. Johnson, Stress evolution due to medium-energy ion bombardment of silicon, Acta Mater. **54**, 483 (2006).
[37] R. L. C. Vink, G. T. Barkema, W. F. van der Weg, and N. Mousseau, Fitting the Stillinger-Weber potential to amorphous silicon, J. Non-Cryst. Solids **282**, 248 (2001).
[38] J. Ziegler, J. Biersack, and U. Littmark, *The Stopping and Range of Ions in Solids* (Pergamon Press, New York, 1985).
[39] R. Biswas, G. S. Grest, and C. M. Soukoulis, Generation of amorphous-silicon structures with use of molecular-dynamics simulations, Phys. Rev. B **36**, 7437 (1987).
[40] W. D. Luedtke and U. Landman, Preparation and melting of amorphous silicon by molecular-dynamics simulations, Phys. Rev. B **37**, 4656 (1988).
[41] M. Ishimaru, S. Munetoh, and T. Motooka, Generation of amorphous silicon structures by rapid quenching: A molecular-dynamics study, Phys. Rev. B **56**, 15133 (1997).
[42] H. J. Berendsen, J. P. M. Postma, W. F. van Gunsteren, A. DiNola, and J. R. Haak, Molecular dynamics with coupling to an external bath, J. Chem. Phys. **81**, 3684 (1984).
[43] M. Moseler, P. Gumbsch, C. Casiraghi, A. C. Ferrari, and J. Robertson, The ultrasmoothness of diamond-like carbon surfaces, Science **309**, 1545 (2005).
[44] M. Castro, R. Gago, L. Vazquez, J. Munoz-Garcia, and R. Cuerno, Stress-induced solid flow drives surface nanopatterning of silicon by ion-beam irradiation, Phys. Rev. B **86**, 214107 (2012).
[45] S. Norris, M. Brenner, and M. Aziz, From crater functions to partial differential equations: A new approach to ion bombardment induced nonequilibrium pattern formation, J. Phys. Condens. Matter **21**, 224017 (2009).
[46] M. Castro and R. Cuerno, Hydrodynamic approach to surface pattern formation by ion beams, Appl. Surf. Sci. **258**, 4171 (2012).
[47] R. M. Bradley, Dynamic scaling of ion-sputtered rotating surfaces, Phys. Rev. E **54**, 6149 (1996).
[48] C. C. Umbach, R. L. Headrick, and K.-C. Chang, Spontaneous nanoscale corrugation of ion-eroded SiO_2: The role of ion-irradiation-enhanced viscous flow, Phys. Rev. Lett. **87**, 246104 (2001).
[49] S. Vauth and S. G. Mayr, Relevance of surface viscous flow, surface diffusion, and ballistic effects in keV ion smoothing of amorphous surfaces, Phys. Rev. B **75**, 224107 (2007).
[50] M. L. Nietiadi and H. M. Urbassek, Influence of local curvature on sputtering, Appl. Phys. Lett. **103**, 113108 (2013).